Published in final edited form as:
Bone. 2009 August ; 45(2): 346–356. doi:10.1016/j.bone.2009.04.251.

Mecp2 Deficiency Decreases Bone Formation and Reduces Bone Volume in a Rodent Model of Rett Syndrome

R.D. O'Connor[1], **M. Zayzafoon**[2], **M.C. Farach-Carson**[1,3,4], and **N.C. Schanen**[1,5]

[1] Department of Biological Sciences, University of Delaware, Newark, DE 19716

[2] Department of Pathology, University of Alabama at Birmingham, Birmingham, AL, 35294

[3] Department of Materials Sciences and Engineering, University of Delaware, Newark, DE 19716

[4] Center for Translational Cancer Research, University of Delaware, Newark, DE 19716

[5] Human Genetics Research Laboratory, Center for Pediatric Research, Nemours Biomedical Research, A.I. duPont Hospital for Children, Wilmington, DE, 19803

Abstract

Rett Syndrome (RTT), a neurological disorder characterized by neurological impairment and a high frequency of osteopenia which often manifests early in childhood, most often is caused by inactivating mutations in the X-linked gene encoding a regulator of epigenetic gene expression, methyl CpG binding protein, MeCP2. Clinical data show that, along with neurological defects, females with RTT frequently have marked decreases in *B*one *M*ineral *D*ensity (BMD) beyond that expected from disuse atrophy. To investigate the relationship between loss of Mecp2 and reduced BMD, we used a *Mecp2* null mouse model, *Mecp2*$^{-/yBIRD}$, for our histological and biochemical studies. *Mecp2*$^{-/yBIRD}$ mice have significantly shorter femurs and an overall reduced skeletal size compared to wild-type mice by post-natal day 60 (P60). Histological and histomorphometric studies identified growth plate abnormalities as well as decreased cortical and trabecular bone in P21 and especially in P60 *Mecp2*$^{-/yBIRD}$ mice. Dynamic histomorphometry revealed decreased Mineral Apposition Rates (MAR) in Mecp2 null femoral trabecular bone as well as in calvarial bone samples. While changes in MAR of cortical bone were not significant, loss of Mecp2 significantly reduced cortical, trabecular and calvarial bone volume compared with age-matched wild-type animals. These differences indicate that Mecp2 deficiency leads to osteoblast dysfunction, which translates into reduced osteoid deposition accounting for the reduced bone volume phenotype. While individual variations were observed in OPG and Rankl concentrations, molar ratios of OPG:Rankl at P21 and P60 were comparable between wild-type and *Mecp2*$^{-/yBIRD}$ mice and showed a consistent excess of OPG. In tibial sections, TRAP staining demonstrated equivalent osteoclast number per bone surface measurements between wild-type and null animals. Our work with a *Mecp2* null mouse model suggests epigenetic regulation of bone in the *Mecp2*$^{-/yBIRD}$ mice which is associated with decreased osteoblast activity rather than increased osteoclastic bone loss.

†Corresponding Author: Laboratory for Human Genetics, Nemours/A.I. duPont Hospital for Children, Wilmington, DE, 19803, Tel: 302-651-6702, Fax: 302-651-6767, Email: schanen@medsci.udel.edu.

Introduction

Over 95% of all patients with the neurodevelopmental disorder, Rett syndrome (RTT), are females who present with neurological dysfunction that becomes apparent after the first few months of life [1,2]. In addition to the prominent neurological symptoms, children with RTT frequently have reductions in skeletal growth and low BMD, which lead to pathological fractures in childhood and early adolescence [3–5]. While the neurological phenotype of the disorder has been well-characterized, only a handful of clinical reports have focused on describing the skeletal phenotype in this patient population. One of the first studies to document the risk of osteopenia in RTT compared bone mineralization in RTT girls with normal controls and individuals diagnosed with Cerebral Palsy (CP), who have impaired mobility and risks for disuse atrophy similar to patients with RTT [3]. In this study, the RTT patients ranged in age from 2–20 years with a mean age of 8.6 years, while the mean age of CP patients and normal females was 12.1 and 10.5 years, respectively. Despite adequate calcium and vitamin D intake, RTT patients in comparison to both control populations had decreases in whole body and spinal BMD as well as BMC (Bone Mineral Content) even when corrected for age. Longitudinal and cross-sectional studies of RTT patients revealed that while bone mass does increase over time in RTT girls, it does so at a much lower rate than in normal controls [6–9]. The reduction in cortical bone thickness and BMD is further exacerbated by anticonvulsant use, immobility and scoliosis, which compound the morbidity imparted by bone fragility in RTT patients [10–13].

Most cases of RTT are caused by mutations in *MECP2* (murine ortholog *Mecp2*), encoding a methyl CpG binding protein [14]. Mecp2 is the most notable in a family of methyl binding domain proteins that all share sequence homology with the methyl binding domain (MBD) of Mecp2 [15–17]. In addition to the MBD, a transcriptional repression domain (TRD) [18] and nuclear localization signal (NLS) have been identified. DNA methylation of cytosines in CpG dinucleotides is an epigenetic modification that is important for transcriptional regulation [19–21], X chromosome inactivation [22], and imprinting [23]. Mecp2 was identified as a protein that would preferentially bind methylated CpG dinucleotides [17,24] in the genome and repress transcription by recruiting co-repressors such as mSin3A, c-Ski, N-CoR [25] as well as histone deacetylases [26,27], although there is evidence that Mecp2 can repress transcription independent of methylation state [28]. Until recently, it was believed that Mecp2 acted solely as a global transcriptional repressor, even though microarray analyses using Mecp2 deficient systems did not yield much information regarding specific targets of Mecp2 [29–31]. Recent studies have demonstrated that Mecp2 binding is not limited to promoter regions of genes [32], nor is Mecp2 now confined to its role as a long-term transcriptional silencer. Further work has shown that Mecp2 has the ability to bind and transcriptionally regulate genes through both transcriptional repression and activation, and that CREB is a transcriptional target of Mecp2 repression [33]. These studies complement the hypothesis that the Mecp2 protein has multiple functions, which may include acting as a chromatin architectural protein (reviewed in [34,35]).

Several Mecp2 deficient rodent models have been developed that harbor various inactivating mutations in the *Mecp2* locus. The strain developed by the Bird laboratory, B6.129P2(C)-Mecp2tm1.1Bird/J, carries a deletion of exons 3 and 4 generated by a constitutive Cre-mediated recombination event [36]. The line is carried through heterozygous females and all studies were performed using the hemizygous males ($Mecp2^{-/yBIRD}$) because individual differences in X-inactivation patterns in females lead to marked variability in phenotype. While extensive work has established many neurological similarities between this mouse model and RTT patients, we sought to determine if this mouse model would recapitulate the bone phenotype and provide insight into the mechanism by which Mecp2 regulates BMD. To eliminate any potential artifacts resulting from secondary effects owed to neurological deficits in feeding or activity, only the mildly to moderately symptomatic animals were included in this study.

Material and Methods

Animal Care and Use

Female B6.129P2(C)-Mecp2tm1.1Bird/J mice developed by the Bird laboratory, which are heterozygous for the *Mecp2* gene, were obtained from Jackson Laboratory in addition to wild-type C57Bl/6J male mice [36]. Although the strain was originally developed on a mixed background, it has undergone extensive numbers of backcrosses and now is congenic to the C57Bl/6J strain. Subsequent breeding and genotyping were performed at the A.I. duPont Hospital for Children/Nemours Foundation Life Science Center. Mice were supplied with water and standard mouse chow ad libitum. Heterozygous breeding female diets were supplemented with sunflower seeds [37], dried banana chips, and Supreme MiniTreats (Bio-Serv) to enhance maternal care of new litters. All subsequent studies were performed using the hemizygous males ($Mecp2^{-/yBIRD}$, $n \geq 4$ for each timepoint) following procedures approved by the IACUC at the A.I. duPont Hospital for Children/Nemours Foundation or University of Delaware, as appropriate. When possible, littermates were used in the following studies.

In addition to the progressive growth deficiency exhibited by $Mecp2^{-/yBIRD}$ mice between P21 and P60, they also developed behaviors that included rapid breathing and short periods of "freezing" becoming more frequent as the mice aged. To minimize potentially confounding variables introduced by the neurological symptoms, all P21 mice (weight range 4.4–11.1g) used in the following studies were healthy and active and the P60 *Mecp2* null mice (weight range 11.7–29.4g), although symptomatic, were also lively and active. The behavioral abnormalities exhibited by symptomatic mice at P60 did not typically lead to extended periods of hypoactivity. The animals selected for the microcomputed tomography (μCT) and histological analyses were all nourished, mobile and active and although they were generally smaller (nose to tail) than their wild-type counterparts, their weights were not significantly different than wild-type (Figure 1).

Skeletal Preparations

Skin, organs and other soft tissues including eyes were removed from 8 week old wild-type and *Mecp2* null littermates and the remaining skeletons were fixed overnight in 1% (v/v) acetic acid in 95% (v/v) ethanol. Alcian blue staining used 80ml of 95% (v/v) ethanol + acetic acid + Alcian blue for 72 hours. Dehydration of the skeletons was accomplished in 95% (v/v) ethanol for 24 hours. The solution was changed to 1% (v/v) KOH until the bone became visible after approximately 6 hours and they were stained overnight with Alizarin red. At the end of one week of destaining in a final volume of 20% (v/v) glycerol and 1%(v/v) KOH, dissection of soft tissues was continued. Progressive dehydration in 70% (v/v) ethanol-glycerol (1:1) and then final storage in 100% (v/v) ethanol-glycerol (1:1) was completed before visually capturing the resultant staining patterns.

Bone Histology

Left hind limbs were extracted from wild-type and *Mecp2* null mice at P21 and P60 and fixed for 4–5 days in 4% (w/v) paraformaldehyde. Femurs and tibias were separated and stored in 70% (v/v) ethanol until embedding in paraffin or methyl methacrylate (MMA). Samples were embedded and sectioned in 5μm segments by the Pathology Core Laboratory at the University of Alabama, Birmingham. Hemotoxylin and Eosin (H&E) staining was performed by the standard procedure. Tartrate-Resistent Acid Phosphatase (TRAP) staining was completed using naphthol AS-MX phosphate and fast red TR salt, followed by counterstaining with hemotoxylin. von Kossa staining was accomplished with a 5% (w/v) silver nitrate solution and 20 minute exposure to UV light, followed by washing with 2% (w/v) sodium thiosulfate and counterstain with 1% neutral red. Goldner's Trichrome staining procedure includes several steps beginning with a ferric chloride and hemotoxylin stain, followed by an acidic Ponceau

bath, and phosphomolybdic acid plus Orange G solution before a final incubation in Light Green staining solution. Both H&E and TRAP staining were carried out on proximal tibial sections, which had been decalcified and embedded in paraffin, while von Kossa and Goldner's Trichrome staining were performed on distal femurs that were not decalcified and were embedded in MMA.

Measurement of TRAP Stained Osteoclasts

One TRAP stained tibia section for each sample at P21 and P60 was divided into four quadrants (I–IV) encompassing the growth plate and the primary spongiosum region. The number of TRAP stained cells was independently counted by at least two blinded reviewers, assuming each TRAP stained cell was one osteoclast. Average osteoclast counts were determined for each quadrant and total values for all four quadrants were compared.

To measure the number of osteoclasts per bone surface, one rectangular Region Of Interest (ROI) approximately 200 μm below the growth plate in the proximal spongiosum area was defined in a method adapted from Sawyer et al. [38]. Within the 612.41mm^2 ROI in each tibial section, the surface of the bone was determined by the Image Pro Plus 4.5 manual measurement tool (Leeds Precision Instruments, Inc.). The number of TRAP stained cells was independently counted by two blinded reviewers, assuming each TRAP stained cell was one osteoclast. For each sample, the average number of osteoclasts counted was divided by the surface (mm).

Micro-Computed Tomography (μCT)

Right femurs were removed from P21 and P60 wild-type and *Mecp2* null mice and fixed for 4–5 days in 4% (w/v) paraformaldehyde, followed by storage in 70% (v/v) ethanol. Each femur was scanned at a resolution of 27μm using a GE Healthcare eXplore Locus Pre-Clinical *in vivo* μCT Scanner® (GE Healthcare Bio-Sciences Corp.). Images were reconstructed and analyzed using GE's Microview® software. Femur length was determined by measuring a line drawn at a 90° angle from the distal femur to the proximal femoral head. In P60 wild-type mice, a 2mm region at the mid-diaphysis was used for determination of cortical bone parameters. To control for the smaller size of P60 *Mecp2* null femurs, area and bone content measurements were adjusted for the decreased length of the $Mecp2^{-/yBIRD}$ femur using the calculated average length of the wild-type and nulls. Using the P60 wild-type femur lengths as the control, the Region Of Interest (ROI) for P21 wild-type and *Mecp2* null femurs was adjusted to 1.3mm. In the P21 animals, there was no significant difference in femur length between the wild-type and null animals, so normalization were not necessary for cortical bone measurements. A sampling of P60 femurs was used to determine the lowest threshold value, 2340, which was used as a constant in all subsequent cortical analyses. A threshold of 900 was found to be the lowest value for all P21 bones and therefore used in the cortical analyses of these femurs. 99 to 100 slices at this region allowed for determination of the inner and outer perimeter of cortical bone (mm), marrow, cortical and total area (mm^2), BMD (mg/cm^3) and BMC (mg). Eight measurements of cortical thickness were determined by hand at the mid-shaft of the femurs and averaged to give a single value for each bone. The bone diameter at the mid-diaphysis was measured in both the mediolateral (M/L) and anteroposterior (A/P) direction, as this region of bone is elliptical in shape. A snapshot of each femur was taken at the mid-diaphysis depicting the region where the bone diameters were measured.

In P60 wild-type femurs, trabecular bone analysis was performed on a 1mm ROI in the femoral diaphysis, which was positioned 0.25mm proximal to the residual growth plate. $Mecp2^{-/yBIRD}$ femur analysis was corrected to calculate trabecular bone parameters 0.23mm proximal to the base of the epiphyseal disk in a 0.92mm ROI. At P21, the metaphysis is primarily composed of cartilage; therefore the trabecular analysis was adjusted to capture a 0.5mm ROI beginning proximal to the primary spongiosum transition zone. Trabecular

thresholding was automatically defined by the Microview® software for each individual bone, leading to measurements of volume (mm^3), bone volume (mm^3), BMD and Tissue Mineral Density (TMD, mg/cm^3), and BMC and Tissue Mineral Content (TMC, mg). Using the Microview® software, Isosurfaces were illustrated for representative P60 trabecular bone at the ROI used in the trabecular bone analysis. Snapshots were taken at Isosurface thresholds between 575 and 1000 to visualize the trabecular bone morphology.

Static and Dynamic Histomorphometry

Wild-type and *Mecp2* null mice were double-labeled with calcein on post-natal day 35 and post-natal day 42, and sacrificed on post-natal day 44 or 45 (2–3 days after the final injection). Histology of the distal metaphysis of the left femora was performed by the Histomorphometry and Molecular Analysis Core Laboratory of the Center for Metabolic Bone Disease, University of Alabama at Birmingham. Longitudinal sections (5μm thick) were cut from MMA plastic embedded blocks along the frontal plane and stained with Goldner's Trichrome stain for the static measurements. Additional sections were cut at 10μm, and left unstained for dynamic (fluorescent) measurements. Histomorphometry was performed using the Bioquant Image Analysis System (R&M Biometrics, Nashville, TN)(PMID: 17884821). The measurements, terminology and units used for histomorphometric analysis were those recommended by the Nomenclature Committee of the American Society of Bone and Mineral Research [39]. Measurements were obtained in a cancellous region of bone that measured approximately $2.5mm^2$ which was located 0.5–2.5mm proximally to the epiphyseal growth cartilage of the femurs and contained only secondary spongiosa.

Cross-sectional stained femoral cortical sections were used to determine the static indices while measurements of single-labeled and double-labeled fluorescent surfaces were used for the Mineral Apposition Rate (MAR, μm/day). Static trabecular indices all were measured from the stained femoral sections, while measurements of single-labeled and double-labeled fluorescent surfaces were made in the same region of interest using unstained sections. Static calvarial bone parameters were determined from the stained section of calvaria, and the single-labeled and double-labeled fluorescent surfaces again were used to calculate the MAR. Littermates drawn from three litters were used for these studies. The average weights were as follows: P35: 19.7 +/− 1.7g (WT) and 14.4 +/− 1.8g (Null) $p<0.01$, P42: 21.3 +/− 1.8g (WT) and 15.1 +/− 2.5 (Null) $p<0.01$, and at time of sacrifice: 20.9 +/− 1.6 (WT) and 13.9 +/− 4.0 (Null) $p<0.05$. Animals were not selected for this study based on body weight.

Blood Serum

Blood was obtained via cardiac puncture immediately following euthanization using CO_2 from P21 and P60 male mice. Samples were incubated at room temperature for 1.5 hours, followed by centrifugation at 2000 rcf for 10–20 minutes, which allowed separation of blood serum and red blood cells. The serum was stored at −20°C until assay.

Serum Calcium Concentration

The QuantiChrom Calcium Assay Kit (BioAssay Systems) was used to analyze serum calcium concentrations, with serum (5μl) from each sample assayed in duplicate. In brief, a standard curve was diluted to yield calcium concentrations ranging from 0 to 20 mg/dL. After addition of standard or sample (5μl) to each well of a 96 well plate and 200 μl working reagent, the plate was incubated at room temperature for 3 min. The optical density was measured at 620nm on a standard 96 well plate spectrophotometer. ODsample – ODblank divided by the slope of the standard curve allowed determination of calcium concentration in mg/dL.

Serum Phosphate Concentration

Serum phosphate levels were measured with the QuantiChrom Phosphate Assay Kit (BioAssay Systems) with serum (5μl) from each sample diluted in 45μl distilled water assayed in duplicate in a 96 well plate format. In separate wells, standard (50μl) and blank were transferred while 100μl Kit Reagent was added to all wells. After a 30 minute incubation at room temperature, the optical density was read at 620nm on a standard a 96 well plate spectrophotometer. ODsample-ODblank divided by (ODstandard – ODblank) and then multiplied by 0.28 to give the final phosphate concentrations in mg/dL.

ELISA

Rank ligand/TRANCE/TNFSF11 and Osteoprogerin/TNFRSF11B Enzyme-Linked ImmunoAssays (Quantikine ELISA, R&D systems) provided blood serum levels of Rankl and OPG in P21 and P60 wild-type and *Mecp2*$^{-/yBIRD}$. Serum was diluted 1:2 in Calibrator Diluent for Rankl ELISA and 1:5 in Calibrator Diluent for OPG ELISA and each sample was assayed in duplicate. Following manufacturer instructions, the absorbance was read at 450nm with a wavelength correction at 570nm on a standard 96 well plate spectrophotometer. Rankl and OPG concentration was determined by ODsample – ODblank multiplied by the appropriate dilution factor and plotted against a standard curve to obtain the concentration in pg/mL. The molar ratios were calculated using the median value of each group of samples and a molecular mass of 43.52 kDa for OPG and 21.36 kDa for Rankl (SwissProt).

Statistical Analysis

Data is presented as the average +/− standard deviation, and unpaired t tests performed with the Graph Pad analysis Software were used to determine statistical significance between wild-type and *Mecp2*$^{-/yBIRD}$ samples. Statistical significance was set at an alpha of $p<0.05$ for all studies.

Results

The *Mecp2*$^{-/yBIRD}$ mice showed postnatal growth retardation when compared to age-matched C57Bl/6J wild-type male mice. *Mecp2*$^{-/yBIRD}$ and wild-type littermates were indistinguishable from birth through P21, after which the size difference in *Mecp2*$^{-/yBIRD}$ mice became apparent. Between 3 and 5 weeks of age, the small stature and curved spine of the *Mecp2* null mice became obvious (Figure 1A and 1B), with both phenotypes becoming more pronounced as the animals aged. Even though the weights of the animals used for these studies at both time points were comparable (Figure 1C), the mutant mice often had a visibly reduced skeletal size as depicted in Figure 1D. The basis for this apparent discrepancy was the observation that the *Mecp2* null males often had more subcutaneous fat than their wild-type counterparts detected during the dissection process. The kyphotic 'C' curvature of the spine was apparent in P60 live animals (Figure 1A and 1B), as well as in Alcian blue and Alizarin red stained skeletal preparations at P60 (Figure 1D). While progressive growth deficiency in the *Mecp2*$^{-/yBIRD}$ mice between P21 and P60 and spinal curvature in the living mice were evident, skeletal preparations stained with Alcian blue and Alizarin red did not show an obvious difference in either bone matrix mineralization or cartilage content.

Histological studies of *Mecp2* null and wild-type tibias and femurs revealed several differences in bone phenotype at P21 and P60. H&E staining of decalcified paraffin-embedded tibia sections in P21 *Mecp2*$^{-/yBIRD}$ mice (Figure 2A) depicted a shortened growth plate in the proximal tibia as well as evidence for abnormally condensed columnar chondrocytes and hypertrophic chondrocytes within the growth plate. Moreover, the zone of hypertrophic chondrocytes at the base of the chondro-osseous junction was thinner in the *Mecp2* null mouse sections, compared to the thickness of the whole growth plate. The newly formed trabeculae

within the primary spongiosum had a distinctly different morphology in the *Mecp2*$^{-/yBIRD}$ mouse compared with wild-type controls. At the base of the growth plate, the trabeculae were thinner, but increased in number, while in the secondary spongiosum the trabeculae were sparser, thicker and more widely spaced. Additionally, there was visible hypercellularity of the bone marrow compartment of the primary spongiosia of the *Mecp2*$^{-/yBIRD}$ animals, an area that contains precursor cells including mesenchymal and hematopoetic stem cells as well as red blood cells and adipocytes.

Examination of tibial sections of P60 *Mecp2* null mice stained with H&E (Figure 2B) showed progression of many of the same observations noted in younger mice. Although the growth plate at P60 showed the expected age-related shortening, the residual growth plates of the *Mecp2*$^{-/yBIRD}$ mice were considerably shorter than those in the wild-type animals. The columnar chondrocytes within the growth plate remained abnormally arranged, with a marked decrease in the zone of hypertrophy. The osteopenic primary spongiosum was characterized by a dramatic deficiency in trabeculae compared to the wild-type sections. The irregular morphology of the trabeculae with long, thin spicules in wild-type trabecular bone and short, thicker trabeculae in null samples, made it difficult to compare trabecular numbers on a histological section. However, it was obvious that the overall amount of *Mecp2* null trabecular bone was markedly decreased by P60. The hypercellularity of the marrow area persisted and appeared to increase between P21 and P60 in the *Mecp2* null mice. Furthermore, we observed an increase in circular unstained regions in both the epiphysis and the proximal diaphysis in P60 *Mecp2* null mice, which may be indicative of an increase in the number of adipocytes. The number of unstained regions was not as apparent in the P21 bones.

von Kossa and Goldner's Trichrome stain were used to differentiate calcium salts and mineralized tissue in undecalcified distal femurs from P21 and P60 wild-type and *Mecp2* null mice (Figure 2C–D). At P21, von Kossa staining labeled less mineralized tissue in both the primary and secondary spongiosum, which is indicative of reduced hydroxyapatite crystals in bone of null animals. Both the cancellous bone shape and quantity of the bone were different in *Mecp2* null mice compared with wild-type. The null mice had fewer trabeculae in the diaphysis in the region proximal to the growth plate, which is consistent with the trabecular bone structure seen in the H&E stains. By P60, the lack of trabecular structure near the residual growth plate and in the proximal epiphysis was even more pronounced than at P21. Similar results were seen when Goldner's Trichrome was used to detect mineralized bone matrix, in both the P21 and P60 animals. Additionally, the width of the femoral cortical bone was slightly thinner in the P21 *Mecp2* null mouse in contrast with the wild-type, and a decrease in cortical thickness became even more obvious by the time the mice had reached 60 days of age. Taken together, the histological studies provide clear evidence that both trabecular and cortical bone are abnormal in *Mecp2* deficient mice. TRAP staining for osteoclasts did not reveal a difference in the absolute number or the number of osteoclasts per bone surface at P21 or P60 (Figure 3A–C), suggesting that *Mecp2*$^{-/yBIRD}$ mice and wild-type controls have similar bone resorption capacities.

μCT analysis was used to examine the three-dimensional structure of wild-type and *Mecp2* null mouse femurs in animals at both ages. *Mecp2*$^{-/yBIRD}$ and wild-type femurs were comparable in length at P21 but by P60, *Mecp2* null femurs were significantly shorter ($p<0.005$) than their age-matched counterparts (Figure 4). These morphometrical comparisons revealed considerable differences in cortical bone parameters by P60, while several trends were noteworthy in the trabecular bone. Figure 5A depicts the typical mid-diaphysis cortical bone of the tibia at P21 and P60 in the *Mecp2* null and wild-type mouse. At P21 no obvious differences were noted between the *Mecp2*$^{-/yBIRD}$ and wild-type cortical bone. However, by P60 there was a visible decrease in the thickness of the cortical bone in the *Mecp2* null tibias. These observations complement the two-dimensional histology data suggesting a reduction in

cortical bone thickness. The three-dimensional representation of P60 trabecular bone (Figure 5B) was depicted through a snapshot of the trabecular bone ROI used in the μCT study. From the images of the *Mecp2* null femurs, less trabecular bone was noted and small gaps in the trabeculae became visible even though comparable thresholding parameters were used. Additionally, in the *Mecp2*$^{-/yBIRD}$ samples it was obvious that the trabecular bone structure was different, as the bones appeared to have increased number of smaller trabecular spicules.

At P21, *Mecp2*$^{-/yBIRD}$ and wild-type femurs were similar in most measures, although trends in growth parameters and cortical thickness were present at this age that continued or became even more pronounced in P60 femurs. By P60, disparities similar to those detected histologically in the tibias were apparent between wild-type and *Mecp2* null femurs in the cortical bone at the mid-diaphysis (Table 1). *Mecp2* null femurs had a smaller outer perimeter ($p<0.05$), but not inner perimeter, of cortical bone, and accordingly the cortical thickness of these bones also was thinner. The marrow area, cortical area, and total area were significantly decreased ($p<0.05$, $p<0.01$ and $p<0.01$, respectively) in *Mecp2*$^{-/yBIRD}$ femurs, along with both the M/L and A/P bone diameters (both $p<0.05$), all measured at the mid-diaphysis. While BMD was not significantly decreased in the null femurs, the trend shows that it was lower than wild-type at both P21 and P60. BMC, however, was different from P21 samples in that it was significantly reduced in P60 *Mecp2* null femurs ($p<0.01$). Cortical thickness and BMC, along with marrow area, cortical area, and total area all were disproportionately lower than would be expected for a bone that is 92% the length of the age-matched wild-type. The cortical bone analysis is consistent with the histology results at both P21 and P60. Notably, these analyses did not detect clear differences between trabecular bone properties of *Mecp2*$^{-/yBIRD}$ and wild-type mice (Table 1). At both P21 and P60, BMD, BMC, TMD, and TMC were modestly lower in *Mecp2* null femurs, but these decreases did not reach statistical significance with the number of animals that we had available for this study.

Results of the histomorphological study, including static and dynamic measurements of cortical and trabecular bone as well as several static and dynamic parameters assessed from calvaria, are listed in Table 2. In the cross-sectional cortical bone analysis of the femurs, the *Mecp2* null mice had significantly decreased cross-sectional cortical ($p<0.01$) and marrow area ($p<0.05$) as well as cortical wall thickness ($p<0.01$), consistent with the results of the μCT study. Bone Area/Tissue Area ($p<0.05$) and trabecular thickness ($p<0.01$) were significantly decreased in the *Mecp2* null trabeculae. Interestingly, the number of osteoblasts and the osteoblast perimeter measurement was similar between the wild-type and *Mecp2* null samples. Mineral apposition rate (MAR) ($p<0.01$) was also reduced by over 30% in *Mecp2*$^{-/yBIRD}$ femurs. Moreover, the number of osteoblasts/bone surface ($p<0.05$) and the MAR ($p<0.05$) were significantly decreased by 55% and 22%, respectively in the calvaria of *Mecp2*$^{-/yBIRD}$ samples, while analyses of osteoid thickness and calvarial wall thickness did not reveal major differences. Taken together these quantitative measures of bone structure and formation in cortical, trabecular, and calvarial bone point to osteoblast dysfunction as the primary cause of the reduced bone volume phenotype observed in Rett Syndrome.

Serum levels of OPG and Rankl (Figure 6) were assessed from P21 and P60 wild-type and *Mecp2* null male mice by ELISA. The results of the Rankl ELISA show a relative increase in Rankl concentration in *Mecp2* null mice at P21, while lower Rankl levels were evident by P60, although notably, individual animals showed both high and low levels of serum Rankl at each age. A slight decrease in OPG levels of P21 *Mecp2* null mice was noted, but this decrease did not became significant ($p<0.05$) until 60 days of age. Molar ratios of OPG and Rankl at P21 and P60 showed a consistent excess of OPG. The OPG:Rankl molar ratio in both wild-type and *Mecp2* null samples decreased from P21 to P60 respectively, as expected for adult mice nearing the end of their maturation growth spurt. Serum calcium and phosphate levels were comparable between wild-type and *Mecp2* null mice at both P21 and P60 (data not shown).

Discussion

The results of our work reveal that *Mecp2*$^{-/yBIRD}$ mice have an abnormal skeletal phenotype that shares many of the components of the clinical skeletal features of RTT patients, who often develop early onset decreased BMD, which becomes increasingly severe in adolescence and adulthood. Our studies using a Mecp2 deficient animal model demonstrate that *Mecp2*$^{-/yBIRD}$ mice have a reduced skeletal size apparent by P60, along with evidence for a kyphotic curvature of the spine. The observation that *Mecp2*$^{-/yBIRD}$ mice became noticeably smaller than controls as they age is consistent with the short stature evident in RTT patients [40], while the kyphotic posturing frequently observed in the mice is comparable to the 'S'-type scoliotic curvature of the spine that is more common among RTT patients [13,41–44]. In addition to the large variation in the weight of both wild-type and *Mecp2*$^{-/yBIRD}$ mice, the detection of increased subcutaneous fat in many *Mecp2*$^{-/yBIRD}$ mice may explain the comparable weight for the two strains. Notably, other investigators have reported weight gain and changes in fat distribution in mice carrying mutations in this gene [45–47]. Thus, although the mutant and wild-type animals were comparable in weight, the *Mecp2* null mice had considerable reductions in their skeletal growth apparent by P60.

Significant differences in *Mecp2* null mouse cortical bone resulting in reduced cortical thickness and cortical bone diameters also became evident through histological studies and μCT analyses. Cortical bone thinning in *Mecp2* null mouse bones was consistent with what is expected in an osteoporotic model and it is known that reductions in bone strength and increases in cortical microdamage affect the fragility of bone [48]. Complementary histological studies and μCT results revealed an abnormally shaped growth plate along with reduced trabecular bone and irregular morphology of the primary spongiosum in *Mecp2*$^{-/yBIRD}$ tibias. While trends from the μCT results were consistent with much of the observed trabecular bone morphology, they did not reach statistical significance with the number of animals we were able to use for these studies and limitations in the scanning parameters utilized in the μCT analysis. However, the static and dynamic histomorphometric studies provided a more comprehensive investigation into the processes affecting trabecular bone formation and indicate that the trabeculae displayed abnormal diameter and spacing. Previous reports have linked both the loss of trabecular bone as well as increases in trabecular microdamage to osteopenia [49–51], which may provide an explanation for the increased adolescent fractures and reduced BMD observed in RTT [3,4]. Overall decreases in femoral mineralized bone noted through von Kossa and Trichrome staining showed a comparative decrease in P21 *Mecp2* null bone, which became ever more obvious by P60. Reductions in cortical and trabecular bone are consistent with the results from the H&E staining and the μCT, and may account for the increased bone fragility and osteopenia detected in RTT. Thus, the combination of trabecular bone abnormalities and the comparative loss of cortical bone in *Mecp2* null mice are likely to be the cause of the low BMD and increased fractures seen in RTT patients. Significantly shorter femurs and disproportionate reductions in cortical width, cortical area, marrow area, and total area of bone in *Mecp2*$^{-/yBIRD}$ mice suggest that there is a problem with postnatal bone growth and development.

Dynamic histomorphometry using a double calcein label allowed us to explore rates of bone apposition as well as many static measurements of bone at post-natal day 44 (P44) in bone formed either by endochondral or intramembranous ossification. We chose P44 because the bone phenotype becomes apparent between P21 and P60, a time at which the *Mecp2* null mice often manifest severe symptoms. Coincident with differences noted in the μCT analyses, *Mecp2* null femoral cross-sectional cortical and marrow area and the cortical wall thickness were significantly decreased in the fluorescent labeling study. Even though the MAR was not significantly different in this study, the results point to a primary defect in cortical bone wherein the bones are smaller and the cortical bone thickness is decreased. Since cortical and trabecular

bone can be differentially affected by gene mutations and epigenetic factors of bone remodeling, these results are not surprising [52,53].

The significant decreases observed in *Mecp2*$^{-/yBIRD}$ trabecular Bone Area/Tissue Area, and trabecular thickness point toward an osteopenic phenotype that is consistent with our histological data. The increase in Bone Perimeter/Bone Area (data not shown) also correlates with the increase in the number of small trabeculae seen proximal to the epiphyseal plate in the von Kossa staining of *Mecp2*$^{-/yBIRD}$ femurs. While many of the other static parameters of trabecular bone that we measured were similar, it was most interesting to note that there was neither a difference in the number nor size of the osteoblasts in this bone type. From this data and the complimentary osteoclast counts on TRAP stained tibial sections, we conclude that the *Mecp2* null bone phenotype cannot be attributed simply to a cellular imbalance with fewer osteoblasts making bone nor to increased osteoclasts resorbing bone. As occurs in Rett Syndrome patients [6–9], the MAR and bone formation rate/tissue area (data not shown) also was significantly reduced in *Mecp2*$^{-/yBIRD}$ femurs.

Additional investigation of the calvaria showed that the Number of Osteoblasts/Bone Surface and the MAR were significantly decreased in the *Mecp2*$^{-/yBIRD}$ samples, while osteoid thickness and cortical wall thickness were similar. Given that statistical differences were noted in both femur and calvaria, it is unlikely that the mode of ossification plays a role in the bone phenotype of *Mecp2* null mice. Furthermore, these results suggest that the differentiation of osteoblasts in either endochondral or intramembranous bone is not considerably altered in *Mecp2* null mice (O'Connor, unpublished). Given that bone appears to form normally by P21 and the differences in bone phenotype do not become evident until after that, we purport that osteoblast differentiation can occur in the absence of Mecp2, but that sometime after P21 the mature osteoblast is impaired in its continued ability to produce bone matrix. This was clearly reflected in the results of the static and dynamic histomorphometry study at P44. The finding that the osteopenic phenotype is attributable to a primary osteoblast defect is not inconsistent with the previous report of Chen et al. [45] who noted no bone abnormalities in mice with a tissue specific deletion of Mecp2 in brain, but in which Mecp2 would have been wild type in bone.

To assess the secretory function of osteoblasts in wild-type and *Mecp2*$^{-/yBIRD}$ derived osteoblasts, we measured serum levels of OPG and Rankl. The significant decrease in OPG concentration in P60 *Mecp2* null mice was not unexpected as the Rankl levels, although not statistically significant, showed a coincident downward trend from wild-type to *Mecp2*$^{-/yBIRD}$ mice. Despite the fluctuations in the levels of OPG and Rankl, the overall decrease in both the wild-type and *Mecp2* null OPG:Rankl molar ratios from P21 to P60 indicate a normal decrease in modeling as the mice mature into adults. Importantly, due to limitations in the serum sample sizes, individual samples were not always processed for both OPG and Rankl thus; statistical analysis for paired samples from the same animal could not be performed on the OPG:Rankl molar ratios. Another set of biochemical assays that we performed did not reveal alterations in calcium or phosphate homeostasis in the *Mecp2*$^{-/yBIRD}$ mice at either age tested (data not shown). This is consistent with that seen clinically in RTT patients [10,12], who typically have normal serum calcium and phosphate levels. The aforementioned results of the bone phenotype in the *Mecp2* null mouse model are in agreement with several clinical studies that provide evidence for bone mass accretion in RTT patients as they age, but at a reduced rate compared with normal controls [10,12]. Further studies will be needed to identify the exact mechanism by which Mecp2 deficiency diminishes osteoblast function.

Epigenetic regulation of bone is not a new concept, as many groups have reported the correlation of histone deacetylation with regulation of osteoblast differentiation. Clinically, it

has been observed that children with epilepsy [54] as well as adult epilepsy patients [55,56] treated with valproate (VPA), a histone deacetylase inhibitor (HDACi), had a reduction in skeletal growth and bone mass and decreased BMD, respectively. Even though gene profile studies have linked VPA to the up or down-regulation of several sets of genes, the exact mechanism by which VPA accelerates bone differentiation yet ultimately leads to reduced BMD has not yet been elucidated [57,58]. Additionally, there is evidence linking HDACi with accelerated osteoblast differentiation through inhibition of the interaction of HDAC3 and Runx2, a master transcriptional regulator of osteoblast maturation [59,60]. Other studies have highlighted the importance of epigenetic regulation in bone as increased histone 3 acetylation was observed in the bone sialoprotein promoter [61] and both reduced CpG methylation and increased acetylation levels have been implicated in osteocalcin transcriptional activation [62–65]. In one report Mecp2 has been shown to directly bind to a region of the Rankl promoter containing one highly methylated CpG dinucleotide in later passage ST2 cells [66], although the direct effect of Mecp2 binding on Rankl transcriptional regulation has not been confirmed. Because both methylation and acetylation can change the epigenome, it is possible that loss of Mecp2 has similar mechanisms of regulating BMD and osteoblast differentiation.

From this study we determined that there is a deficiency in bone volume that becomes evident post-natally, before the onset of neurological symptoms in *Mecp2*$^{-/yBIRD}$ mice. These results indicate that the bone phenotype in RTT is not primarily a disuse phenomenon as has been speculated upon. The reduced bone volume and abnormal morphology evident in *Mecp2*$^{-/yBIRD}$ mice suggest a fundamental defect in the function of the osteoblast. Use of the *Mecp2* null mouse model will allow us to further investigate the epigenetic regulation of bone homeostasis and mechanistically study the effect of Mecp2deficiency on osteoblast function..

Acknowledgments

This work would not be possible without the help of the following people and funding from Nemours, NIH COBRE P20 RR016458-06 (MCFC) and NIH COBRE P20 RR020173-04 (NCS). The authors would like to gratefully acknowledge Andrea Ham, Marvin Kendell, and the A.I. duPont Hospital for Children Life Sciences Center for their tremendous help with genotyping and animal husbandry. We sincerely thank Christopher Price, Catherine Kirn-Safran, Laura Sloofman, Rob Long and Aaron Wolff for their assistance with the μCT studies and analysis. Additionally we would like to thank Genevieve Laforet (UMass) for sending us animals for the skeletal preparations as well as Svilen Bobev for generously lending his technical expertise in bone mineralization analysis. The authors greatly appreciate helpful suggestions from Randall Duncan, George Dodge, and the efforts of the Histochemistry Core Laboratory at the A.I. duPont Hospital for Children and the CMBD Core Laboratory at the University of Alabama, Birmingham. We also appreciate the efforts of the TRAP cell counters: Ben Isreal, Kyle Green, Swati Pradham and Jessica Malin.

References

1. Hagberg B, Aicardi J, Dias K, Ramos O. A progressive syndrome of autism, dementia, ataxia, and loss of purposeful hand use in girls: Rett's syndrome: report of 35 cases. Annals of Neurology 1983;14(4): 471–479. [PubMed: 6638958]
2. Hagberg B. Rett's syndrome: prevalence and impact on progressive severe mental retardation in girls. Acta Paediatr Scand 1985;74(3):405–8. [PubMed: 4003065]
3. Haas RH, et al. Osteopenia in Rett syndrome. J Pediatr 1997;131(5):771–4. [PubMed: 9403666]
4. Leonard H, et al. A population-based approach to the investigation of osteopenia in Rett syndrome. Dev Med Child Neurol 1999;41(5):323–8. [PubMed: 10378758]
5. Leonard H, et al. Skeletal abnormalities in Rett syndrome: increasing evidence for dysmorphogenetic defects. Am J Med Genet 1995;58(3):282–5. [PubMed: 8533832]
6. Zysman L, Lotan M, Ben-Zeev B. Osteoporosis in Rett syndrome: A study on normal values. ScientificWorldJournal 2006;6:1619–30. [PubMed: 17173180]
7. Budden SS, Gunness ME. Bone histomorphometry in three females with Rett syndrome. Brain Dev 2001;23(Suppl 1):S133–7. [PubMed: 11738859]

8. Budden SS, Gunness ME. Possible mechanisms of osteopenia in Rett syndrome: bone histomorphometric studies. J Child Neurol 2003;18(10):698–702. [PubMed: 14649552]
9. Motil KJ, et al. Bone Mineral Content and Bone Mineral Density Are Lower in Older than in Younger Females with Rett Syndrome. Pediatr Res. 2008
10. Gonnelli S, et al. Bone ultrasonography at phalanxes in patients with Rett syndrome: A 3-year longitudinal study. Bone 2008;42(4):737–42. [PubMed: 18242156]
11. Cepollaro C, et al. Dual X-ray absorptiometry and bone ultrasonography in patients with Rett syndrome. Calcif Tissue Int 2001;69(5):259–62. [PubMed: 11768194]
12. Motil KJ, et al. Fractional calcium absorption is increased in girls with Rett syndrome. J Pediatr Gastroenterol Nutr 2006;42(4):419–26. [PubMed: 16641581]
13. Keret D, et al. Scoliosis in Rett syndrome. J Pediatr Orthop 1988;8(2):138–42. [PubMed: 3350946]
14. Amir RE, et al. Rett syndrome is caused by mutations in X-linked MECP2, encoding methyl-CpG-binding protein 2. Nat Genet 1999;23(2):185–8. [PubMed: 10508514]
15. Meehan RR, et al. Identification of a mammalian protein that binds specifically to DNA containing methylated CpGs. Cell 1989;58(3):499–507. [PubMed: 2758464]
16. Meehan RR, Lewis JD, Bird AP. Characterization of MeCP2, a vertebrate DNA binding protein with affinity for methylated DNA. Nucleic Acids Research 1992;20(19):5085–92. [PubMed: 1408825]
17. Nan X, Meehan RR, Bird A. Dissection of the methyl-CpG binding domain from the chromosomal protein MeCP2. Nucleic Acids Research 1993;21(21):4886–92. [PubMed: 8177735]
18. Nan X, Campoy FJ, Bird A. MeCP2 is a transcriptional repressor with abundant binding sites in genomic chromatin. Cell 1997;88(4):471–81. [PubMed: 9038338]
19. Chen WG, et al. Derepression of BDNF transcription involves calcium-dependent phosphorylation of MeCP2. Science 2003;302(5646):885–9. [PubMed: 14593183]
20. Darwanto A, et al. MeCP2 and promoter methylation cooperatively regulate E-cadherin gene expression in colorectal carcinoma. Cancer Sci 2003;94(5):442–7. [PubMed: 12824891]
21. Drewell RA, et al. Methylation-dependent silencing at the H19 imprinting control region by MeCP2. Nucleic Acids Res 2002;30(5):1139–44. [PubMed: 11861904]
22. Jeppesen P, Turner BM. The inactive X chromosome in female mammals is distinguished by a lack of histone H4 acetylation, a cytogenetic marker for gene expression. Cell 1993;74(2):281–9. [PubMed: 8343956]
23. Pedone PV, et al. Role of histone acetylation and DNA methylation in the maintenance of the imprinted expression of the H19 and Igf2 genes. Febs Letters 1999;458(1):45–50. [PubMed: 10518931]
24. Nan X, et al. DNA methylation specifies chromosomal localization of MeCP2. Mol Cell Biol 1996;16 (1):414–21. [PubMed: 8524323]
25. Kokura K, et al. The Ski protein family is required for MeCP2-mediated transcriptional repression. J Biol Chem 2001;276(36):34115–21. [PubMed: 11441023]
26. Jones PL, et al. Methylated DNA and MeCP2 recruit histone deacetylase to repress transcription. Nature Genetics 1998;19(2):187–91. [PubMed: 9620779]
27. Nan X, et al. Transcriptional repression by the methyl-CpG-binding protein MeCP2 involves a histone deacetylase complex [see comments]. Nature 1998;393(6683):386–9. [PubMed: 9620804]
28. Georgel PT, et al. Chromatin compaction by human MeCP2. Assembly of novel secondary chromatin structures in the absence of DNA methylation. J Biol Chem 2003;278(34):32181–8. [PubMed: 12788925]
29. Colantuoni C, et al. Gene expression profiling in postmortem Rett Syndrome brain: differential gene expression and patient classification. Neurobiol Dis 2001;8(5):847–65. [PubMed: 11592853]
30. Traynor J, et al. Gene expression patterns vary in clonal cell cultures from Rett syndrome females with eight different MECP2 mutations. BMC Med Genet 2002;3:12. [PubMed: 12418965]
31. Tudor M, et al. Transcriptional profiling of a mouse model for Rett syndrome reveals subtle transcriptional changes in the brain. Proc Natl Acad Sci U S A 2002;99(24):15536–41. [PubMed: 12432090]

32. Yasui DH, et al. Integrated epigenomic analyses of neuronal MeCP2 reveal a role for long-range interaction with active genes. Proc Natl Acad Sci U S A 2007;104(49):19416–21. [PubMed: 18042715]
33. Chahrour M, et al. MeCP2, a key contributor to neurological disease, activates and represses transcription. Science 2008;320(5880):1224–9. [PubMed: 18511691]
34. Chadwick LH, Wade PA. MeCP2 in Rett syndrome: transcriptional repressor or chromatin architectural protein? Curr Opin Genet Dev 2007;17(2):121–5. [PubMed: 17317146]
35. Clouaire T, Stancheva I. Methyl-CpG binding proteins: specialized transcriptional repressors or structural components of chromatin? Cell Mol Life Sci. 2008
36. Guy J, et al. A mouse Mecp2-null mutation causes neurological symptoms that mimic Rett syndrome. Nature Genetics 2001;27(3):322–326. [PubMed: 11242117]
37. Jugloff DG, Logan R, Eubanks JH. Breeding and maintenance of an Mecp2-deficient mouse model of Rett syndrome. J Neurosci Methods 2006;154(1–2):89–95. [PubMed: 16439027]
38. Sawyer A, et al. Quantification of tartrate resistant acid phosphatase distribution in mouse tibiae using image analysis. Biotech Histochem 2003;78(5):271–8. [PubMed: 14989645]
39. Parfitt AM, et al. Bone histomorphometry: standardization of nomenclature, symbols, and units. Report of the ASBMR Histomorphometry Nomenclature Committee. J Bone Miner Res 1987;2(6): 595–610. [PubMed: 3455637]
40. Schultz RJ, et al. The pattern of growth failure in Rett syndrome. Am J Dis Child 1993;147(6):633–7. [PubMed: 8506830]
41. Harrison DJ, Webb PJ. Scoliosis in the Rett syndrome: natural history and treatment. Brain Dev 1990;12(1):154–6. [PubMed: 2344012]
42. Holm VA, King HA. Scoliosis in the Rett syndrome. Brain Dev 1990;12(1):151–3. [PubMed: 2344011]
43. Hennessy MJ, Haas RH. The orthopedic management of Rett syndrome. J Child Neurol 1988;3 (Suppl):S43–7. [PubMed: 3198902]
44. Bassett GS V, Tolo T. The incidence and natural history of scoliosis in Rett syndrome. Dev Med Child Neurol 1990;32(11):963–6. [PubMed: 2269405]
45. Chen RZ, et al. Deficiency of methyl-CpG binding protein-2 in CNS neurons results in a Rett-like phenotype in mice. Nat Genet 2001;27(3):327–31. [PubMed: 11242118]
46. Fyffe SL, et al. Deletion of Mecp2 in Sim1-expressing neurons reveals a critical role for MeCP2 in feeding behavior, aggression, and the response to stress. Neuron 2008;59(6):947–58. [PubMed: 18817733]
47. Samaco RC, et al. A partial loss of function allele of methyl-CpG-binding protein 2 predicts a human neurodevelopmental syndrome. Hum Mol Genet 2008;17(12):1718–27. [PubMed: 18321864]
48. Seeman E. Structural basis of growth-related gain and age-related loss of bone strength. Rheumatology (Oxford) 2008;47(Suppl 4):iv2–8. [PubMed: 18556646]
49. McDonnell P, McHugh PE, O'Mahoney D. Vertebral osteoporosis and trabecular bone quality. Ann Biomed Eng 2007;35(2):170–89. [PubMed: 17171508]
50. Dempster DW. The pathophysiology of bone loss. Clin Geriatr Med 2003;19(2):259–70. v–vi. [PubMed: 12916285]
51. Steiniche T. Bone histomorphometry in the pathophysiological evaluation of primary and secondary osteoporosis and various treatment modalities. APMIS Suppl 1995;51:1–44. [PubMed: 7669370]
52. Sakamoto A, et al. Deficiency of the G-protein alpha-subunit G(s)alpha in osteoblasts leads to differential effects on trabecular and cortical bone. J Biol Chem 2005;280(22):21369–75. [PubMed: 15797856]
53. Brennan TC, Rizzoli R, Ammann P. Selective Modification of Bone Quality by PTH, Pamidronate or Raloxifene. J Bone Miner Res. 2008
54. Guo CY, Ronen GM, Atkinson SA. Long-term valproate and lamotrigine treatment may be a marker for reduced growth and bone mass in children with epilepsy. Epilepsia 2001;42(9):1141–7. [PubMed: 11580761]
55. Sato Y, et al. Decreased bone mass and increased bone turnover with valproate therapy in adults with epilepsy. Neurology 2001;57(3):445–9. [PubMed: 11502911]

56. Boluk A, et al. The effect of valproate on bone mineral density in adult epileptic patients. Pharmacol Res 2004;50(1):93–7. [PubMed: 15082034]
57. Schroeder TM, et al. Gene profile analysis of osteoblast genes differentially regulated by histone deacetylase inhibitors. BMC Genomics 2007;8:362. [PubMed: 17925016]
58. Cho HH, et al. Induction of osteogenic differentiation of human mesenchymal stem cells by histone deacetylase inhibitors. J Cell Biochem 2005;96(3):533–42. [PubMed: 16088945]
59. Schroeder TM, et al. Histone deacetylase 3 interacts with runx2 to repress the osteocalcin promoter and regulate osteoblast differentiation. J Biol Chem 2004;279(40):41998–2007. [PubMed: 15292260]
60. Schroeder TM, Westendorf JJ. Histone deacetylase inhibitors promote osteoblast maturation. J Bone Miner Res 2005;20(12):2254–63. [PubMed: 16294278]
61. Lamour V, et al. Runx2- and histone deacetylase 3-mediated repression is relieved in differentiating human osteoblast cells to allow high bone sialoprotein expression. J Biol Chem 2007;282(50):36240–9. [PubMed: 17956871]
62. Shen J, et al. Transcriptional induction of the osteocalcin gene during osteoblast differentiation involves acetylation of histones h3 and h4. Mol Endocrinol 2003;17(4):743–56. [PubMed: 12554783]
63. Villagra A, et al. Reduced CpG methylation is associated with transcriptional activation of the bone-specific rat osteocalcin gene in osteoblasts. J Cell Biochem 2002;85(1):112–22. [PubMed: 11891855]
64. Shen J, et al. Histone acetylation in vivo at the osteocalcin locus is functionally linked to vitamin D-dependent, bone tissue-specific transcription. J Biol Chem 2002;277(23):20284–92. [PubMed: 11893738]
65. Sierra J, et al. Regulation of the bone-specific osteocalcin gene by p300 requires Runx2/Cbfa1 and the vitamin D3 receptor but not p300 intrinsic histone acetyltransferase activity. Mol Cell Biol 2003;23(9):3339–51. [PubMed: 12697832]
66. Kitazawa R, Kitazawa S. Methylation status of a single CpG locus 3 bases upstream of TATA-box of receptor activator of nuclear factor-kappaB ligand (RANKL) gene promoter modulates cell- and tissue-specific RANKL expression and osteoclastogenesis. Mol Endocrinol 2007;21(1):148–58. [PubMed: 17008384]

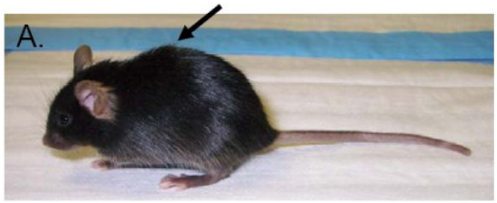

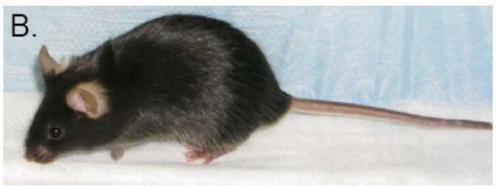

C.

	Average Weight (g)
P21 Wild-type	9.00 +/- 1.75
P21 *Mecp2* $^{-/yBIRD}$	8.28 +/- 0.95
P60 Wild-type	24.30 +/- 2.33
P60 *Mecp2* $^{-/yBIRD}$	22.02 +/- 3.66

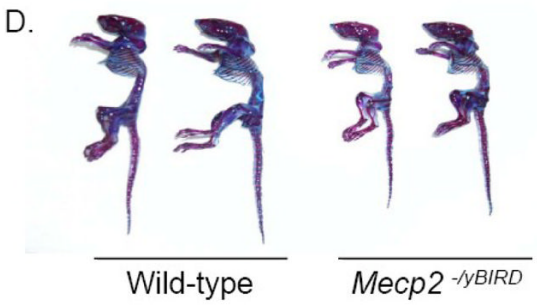

Figure 1. Mecp2$^{-/yBIRD}$ male mice have reduced skeletal size compared with their wild-type littermates by P60

A) Kyphotic posturing in a P60 Mecp2 null male mouse compared with B) an age-matched wild-type control. C) The average body weight of P21 and P60 wild-type and *Mecp2* null male mice used for the histological and μCT evaluations in this study (n≥4). D) Skeletal preparations from P60 wild-type and *Mecp2* null male mice stained with Alcian blue depicting cartilage content (blue) and Alizarin red staining mineralized tissue (red-purple).

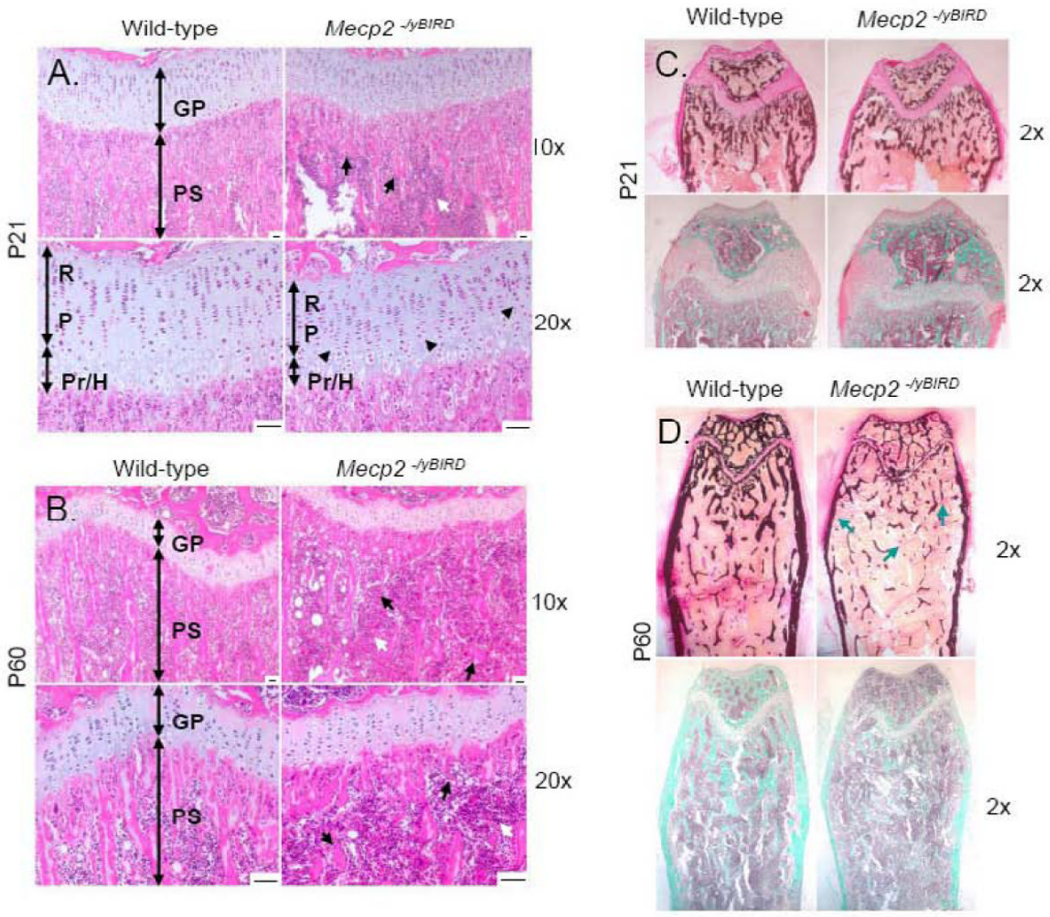

Figure 2. Histological analyses revealed major differences in the growth plate and primary spongiosum of Mecp2$^{-/yBIRD}$ tibias and femurs at P21 and P60

A–B) Hemotoxylin and Eosin (H&E) staining of decalcified paraffin-embedded proximal tibia of P21 and P60 wild-type and *Mecp2* null mice (n≥4). GP, Growth Plate; PS, Primary Spongiosum; R, Resting Zone; P, Proliferating Zone; Pr/H, Pre-hypertrophic/Hypertrophic Zone. Black arrows indicate areas of shortened or abnormal trabecular spicules, whereas black arrowheads show areas of irregularly shaped chondrocytes and columnar structures. White arrows point to regions of hypercellularity. Scale bars = 50μm. C–D) Representative images of undecalcified distal femurs stained with von Kossa (top panels) and Goldner's Trichrome (bottom panels) illustrate calcium deposits (black) and mature bone matrix, as shown with the Trichrome stain (blue-green) in both P21 and P60 mice. Blue arrows indicate reduced cortical and trabecular bone as well as point out tiny fragments of trabeculae in *Mecp2*$^{-/yBIRD}$ sections.

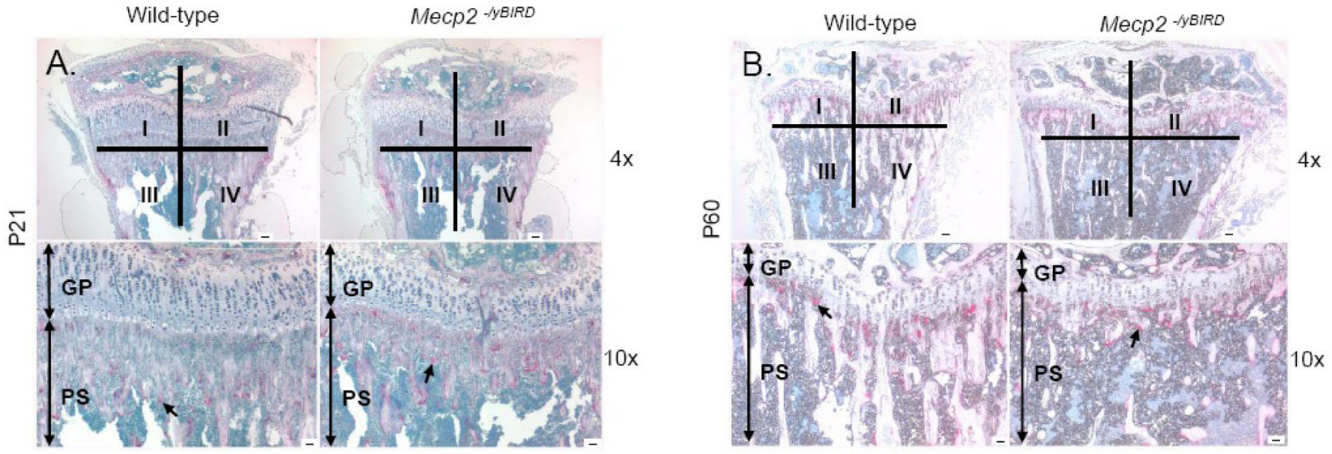

C.

Osteoclast Counts in each Quadrant

	Average I and II	Average III and IV	Average I-IV	No. Osteoclasts/ Bone Surface (mm)
P21 Wild-type	26.65 +/- 7.90	23.25 +/- 5.23	24.95 +/- 8.81	12.55 +/- 4.89
P21 *Mecp2* -/yBIRD	18.65 +/- 10.14	16.70 +/- 9.47	17.68 +/- 7. 51	11.66 +/- 2.63
P60 Wild-type	38.33 +/- 10.30	16.00 +/- 7.28	27.17 +/- 14.37	6.34 +/- 2.43
P60 *Mecp2* -/yBIRD	40.75 +/- 6.42	18.04 +/- 3.89	29.40 +/- 12.67	6.60 +/- 2.30

Figure 3. Similar number of osteoclasts quantified by TRAP staining

A–B) In the decalcified paraffin-embedded tibia, osteoclasts were assessed from representative Tartrate Resistant Acid Phosphatase (TRAP) staining at the base of the growth plate and in the primary spongiosium of P21 and P60 wild-type and *Mecp2* null mice (n≥4). Scale bars = 50μm. Black arrows indicate individual osteoclasts stained for TRAP. Quadrants I–IV that were used for osteoclast quantification are depicted. C) Quantitative measurements of osteoclasts in each quadrant (labeled I–IV) +/− SD, which were determined by TRAP cell counting, and the number of osteoclasts per bone surface (mm) was measured in the primary spongiosum within a constant ROI at both P21 and P60. Values are reported +/− SD.

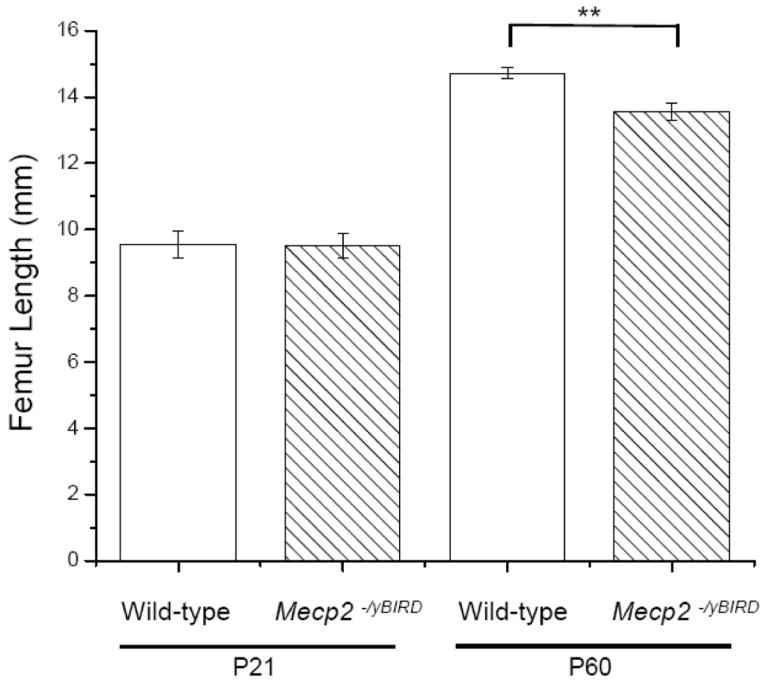

Figure 4. P60 Mecp2$^{-/yBIRD}$ mice had shorter femurs than wild-type controls

Femur length was measured using the μCT Microview® software from bones extracted on P21 and P60 (n≥4). The white columns depict wild-type samples and the hatched white columns indicate *Mecp2*$^{-/yBIRD}$ samples. Average length is shown (mm) +/− SD and the timepoints tested are noted below the graph. Significance was noted ** if $p<0.01$.

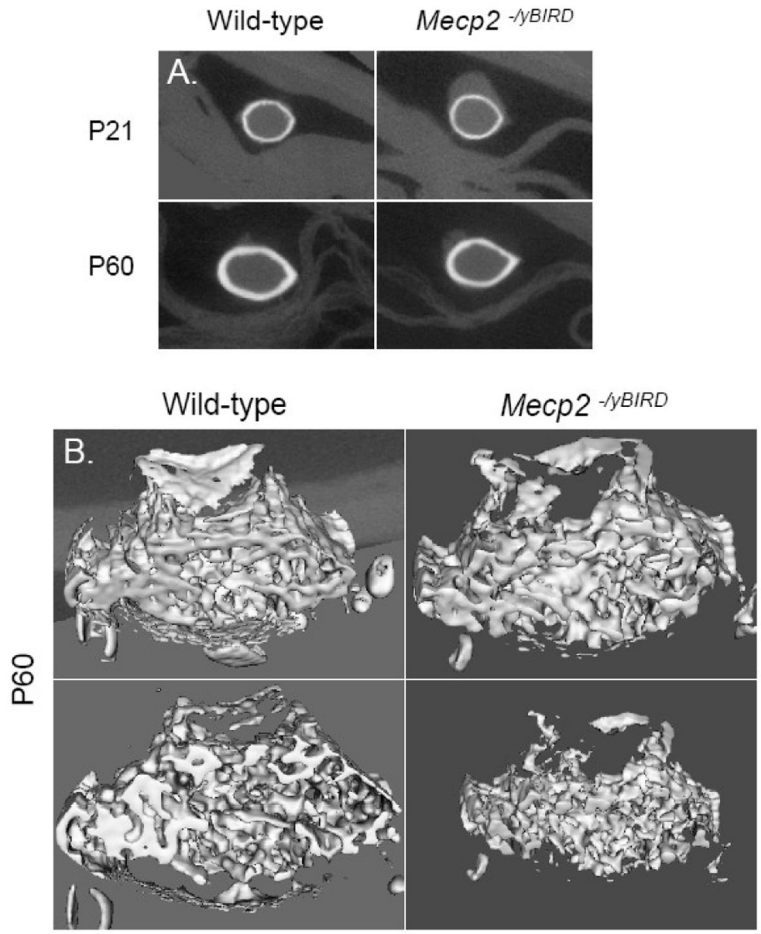

Figure 5. Differences observed in cortical and trabecular bone volumes between Mecp2^{-}/yBIRD and wild-type femurs at P60

A) A characteristic cross-sectional image of cortical bone at the femoral mid-diaphysis of P21 and P60 *Mecp2* null and wild-type mice (n≥4). B) A representative three-dimensional view of the trabecular bone ROI used in the trabecular bone analysis of P60 samples (n≥4).

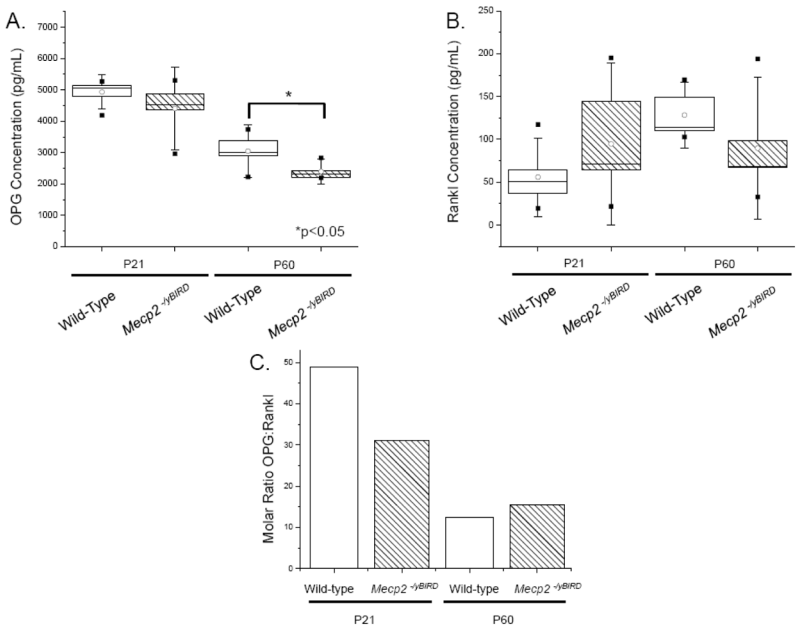

Figure 6. OPG levels were in excess of Rankl at P21 and P60

Duplicate samples of blood serum (n≥6) were assayed by ELISA to determine the concentration of A) OPG and B) Rankl in wild-type and *Mecp2*$^{-/yBIRD}$ mice. Statistical box plot analyses show a range of 25–75%, with the white circle depicting the mean of each group of samples. SD is shown by the whiskers and the high and low values for each set of samples are indicated by [■]. White boxes represent wild-type samples and hatched boxes indicate Mecp2$^{-/yBIRD}$ samples. C) Molar ratios of using the median of OPG and Rankl for each group was calculated and depicted on the graph. White columns represent wild-type samples and hatched white columns indicate *Mecp2*$^{-/yBIRD}$ samples, Significance was noted * if $p<0.05$.

Table 1

μCT revealed cortical bone parameters were decreased in Mecp2 null femurs by P60 and trended lower in trabecular bone of Mecp2$^{-/yBIRD}$ femurs

Mid-diaphysis analysis of cortical bone by microCT was performed using P21 and P60 wild type and Mecp2 null mice as described in Materials and Methods. Trabecular analysis was performed in an ROI selected subjacent to the growth plate (see text).

	P21		P60	
Cortical Bone Parameters	**Wild-type**	***Mecp2*$^{-/yBIRD}$**	**Wild-type**	***Mecp2*$^{-/yBIRD}$**
Inner Perimeter (mm)	3.22 +/− 0.23	3.28 +/− 0.20	3.88 +/− 0.15	3.72 +/− 0.15
Outer Perimeter (mm)	3.81 +/− 0.34	3.85 +/− 0.30	4.76 +/− 0.24	4.37 +/− 0.14*
Cortical Thickness (mm)	0.10+/− 0.01	0.09 +/− 0.01	0.18 +/− 0.02	0.15 +/− 0.01*
Marrow Area (mm^2)	0.78 +/− 0.11	0.81 +/− 0.10	1.08 +/− 0.08	0.93 +/− 0.08*
Cortical Area (mm^2)	0.33 +/− 0.10	0.32 +/− 0.08	0.52 +/− 0.07	0.34 +/− 0.03**
Total Area (mm^2)	1.11+/− 0.20	1.12 +/− 0.17	1.60 +/− 0.13	1.27 +/− 0.07**
M/L Bone Diameter (Width, mm)	1.35 +/− 0.15	1.37 +/− 0.12	1.88 +/− 0.10	1.74 +/− 0.09*
A/P Bone Diameter (Depth, mm)	1.10 +/− 0.09	1.12+/− 0.05	1.26 +/− 0.04	1.20 +/− 0.03*
BMD (mg/cc)	451 +/− 40	433 +/− 50	853 +/− 11	845 +/− 7
BMC (mg)	0.003 +/− 0.001	0.003 +/− 0.001	0.009 +/− 0.001	0.006 +/− 0.001**
Trabecular Bone Parameters				
Volume (mm^3)	0.80 +/− 0.09	0.80 +/− 0.18	1.96+/− 0.18	1.77 +/− .23
Volume of Bone (mm^3)	0.26 +/− 0.04	0.25 +/− 0.02	0.71 +/− 0.04	0.66 +/− 0.09
BMD (mg/cc)	92.74 +/− 15.88	85.88 +/− 16.07	259 +/− 49	221.17 +/− 53.13
BMC (mg)	0.07 +/− 0.01	0.07 +/− 0.01	0.51 +/− 0.10	0.39 +/− 0.08
TMD (mg/cc)	160 +/− 19	145 +/− 10	374 +/− 64	314 +/− 63
TMC (mg)	0.04 +/− 0.01	0.04 +/− 0.003	0.27 +/− 0.05	0.21 +/− 0.05

Results are listed as the average +/− SD for each group of samples (n≥4). Significance was noted * if p<0.05 or ** if p<0.01.

Table 2

Static and dynamic histomorphometry measurements at P44 reveal osteoblast dysfunction in Mecp2 null femurs and calvaria

After calcein double-labeling, stained and unstained bone sections were analyzed in femurs and calvaria of P44 wild-type and *Mecp2*$^{-/yBIRD}$ mice. Goldner's Trichrome stained sections were used for the measurement of static parameters, while unstained fluorescent sections were used for dynamic histomorphometry.

	P44	
Static and Dynamic Histomorphometry	**Wild-type**	***Mecp2*$^{-/yBIRD}$**
Static and Dynamic Cross Section Conical Indices		
Cross-section Cortical Area (mm^2)	0.69 +/− 0.06	0.42 +/− 0.08**
Cross-section Marrow Area (mm^2)	1.26 +/− 0.178	0.94 +/− 0.14*
Mineralizing Surface (MS, mm)	1.31 +/− 0.55	0.74 +/− 0.23
Cortical Wall Thickness (μm)	144.55 +/− 7.05	106.10 +/− 14.91**
Mineral Appsition Rate (MAR, μm/day)	4.11 +/− 0.88	4.73 +/− 1.54
Static and Dynamic Trabecular Indices		
BA/TA (%)	21.33 +/− 1.92	14.06 +/− 458*
Osteoid Perimeter (OS, mm)	1.41 +/− 0.75	1.40 +/− 1.40
Trabecular Thickness (μm)	41.52 +/− 3.12	31.50 +/− 3.51**
Trabecular Number (1/mm)	5.15 +/− 0.50	4.41 +/− 1.09
Trabecular Space (μm)	154.08+/− 17.28	208.78 +/− 65.51
ObS/BS	29.51 +/− 7.23	33.14 +/− 10.28
N.Ob/BS	20.03 +/− 3.01	21.67 +/− 4.19
Mineral Appsition Rate (MAR, μm/day)	1.79 +/− 0.19	1.24 +/− 0.04**
Bone Formation Rate (BFR/BS, (μm/day)	0.61 +/− 0.21	0.43 +/− 0.05
Static and Dynamic Calvarial Indices		
Osteoid Thickness (μm)	4.17+/− 0.53	3.76 +/− 1.29
N.Ob/BS	66.83 +/− 20.74	29.66 +/− 8.09*
Calvaria Wall Thickness (μm)	136.74 +/− 11.60	130.58 +/− 9.74
Mineral Appsition Rate (MAR, μm/day)	1.63 +/− 0.24	1.26 +/− 0.07*

Results are listed as the average +/− SD for each group of samples (n≥4). Significance was noted * if p<0.05 or ** if p<0.01.